Planetary and Space Science 181 (2020) 104782

Contents lists available at ScienceDirect

Planetary and Space Science

journal homepage: www.elsevier.com/locate/pss

Characterization of transient signal induced in IR detector array by Jupiter high-energy electrons and implications for JUICE/MAJIS operability

Pierre Guiot [a,*], Mathieu Vincendon [a], John Carter [a], Yves Langevin [a], Alain Carapelle [b]

[a] IAS, Bâtiment 121, CNRS / Université Paris-Saclay, Orsay, France
[b] CSL, Avenue Du Pré-Aily, Université de Liège, Liège, Belgium

ARTICLE INFO

Keywords:
JUICE
MAJIS
H1RG
Infrared spectral imager
Jupiter radiations
Sofradir retina
Electron transient signal

2019 MSC:
00–01
99-00

ABSTRACT

MAJIS is the visible-infrared spectral imager of the JUICE mission, scheduled by ESA to explore Jupiter and its three icy Galilean moons starting in 2030. It will encounter a challenging environment, the intense Jovian magnetosphere, which among the various expected effects of radiation on detector operability, raises the major issue of transient signal perturbations generated by electrons during every acquisition. This paper aims at a precise characterization of the consequences of such a flux of high-energy electrons on MAJIS detectors in order to evaluate their impact on their operability.

To assess the effects of this environment on MAJIS during the mission, we exposed two candidate detectors for the mission to β^- radioactive sources simulating an environment around the ~ MeV energy. The candidate detectors under tests were Teledyne H1RG and SOFRADIR Retina NGP MWIR with 5.3 μm cut-off. We have developped and validated an algorithm to interpret these measurements and characterize the distribution of electron impacts (or "spikes") both in terms of intensity and spatial distribution.

The main trends we identify are that the Sofradir detector generates in average 1 spike per electron while the H1RG generates in average 2 spikes per electron forming a spatial cluster. The counterpart that we observe is that more energy is deposited in single spikes on the Sofradir than on the H1RG. Yet, the transient signals are of the order of magnitude of 1000 charges in average, filling less than 1% of the full-well capacity of both detectors. Since the foreseen strategy to discriminate the spikes is time filtering on acquisitions that will be split into sub-integrations, the absence of time persistence of the spike signal was paramount and we managed to check its absence on both detectors. We conclude that the expected effects on operability should be effectively mitigated by the foreseen despiking strategy.

1. Introduction

1.1. Jupiter's icy satellites exploration from previous missions

The Jovian system has been previously explored in detail by only two spectro-imaging instruments working in the near infrared: JIRAM on the Juno spacecraft currently orbiting Jupiter and NIMS on Galileo which ended its mission in 2003. While JIRAM primary focus is Jupiter and its atmosphere, NIMS also provided observations of the Galilean Moons surfaces. The NIMS instrument (Carlson et al., 1992) worked in whisk-broom mode with a 1 D detector, using 17 photo-diodes and a rotating grating to cover all wavelengths, while the spatial dimensions were acquired with rotating mirrors and the movement of the spacecraft. The infrared spectra acquired by NIMS exhibit compositional differences, such as on Ganymede (see (McCord et al., 1998)) between regions with exposed water ice on the surface and without. The NIMS data also allowed to derive detailed maps of the surface temperatures of all the Galilean satellites, the distribution of the intense volcanic activity of Io, the detection of ammonia clouds in Jupiter's atmosphere and evidences for the presence of a thin exosphere exhibiting on Europa (de Kleer and Brown, 2018), Ganymede (McGrath et al., 2013) and potentially Callisto (Cunningham et al., 2015).

Other sources of information such as magnetic and gravity field measurements also improved our understanding of the Galilean Moons. After Voyager and Galileo missions, a layer of liquid saline water ocean beneath surface ice crust was suspected on the three icy moons, especially on Europa were its detection is almost certain (Schenk, 2002). The thickness of the surface ice crust is still under debate, it has been

* Corresponding author.
E-mail address: pierre.guiot@ias.u-psud.fr (P. Guiot).

https://doi.org/10.1016/j.pss.2019.104782
Received 18 March 2019; Received in revised form 9 October 2019; Accepted 19 October 2019
Available online 29 October 2019

estimated to 19–25 km for Europa at the end of the Galileo era, and 2–4 times this thickness for Ganymede and Callisto. These inner liquid oceans need to be further confirmed and characterized with orbital analysis, in particular near-IR spectro-imaging at higher spatial and spectral resolution than NIMS (see e.g. (Bagenal et al., 2006)) will notably make it possible to characterize young surfaces, such as Ganymede's which has areas not older than a few hundreds of millions of years according to (Wagner et al., 2018) (still poorly constrained), that are expected to provide information about surface-ocean exchanges. and cryo-volcanic/plume activity, which remain to be thoroughly probed.

Many other science questions remain to be investigated by the future spectro-imaging instrument to explore the Jovian system, such as the question of ocean's composition and potential interactions with the surface for the satellites, but also the origin of the auroras in their exosphere or the exact interaction processes between these bodies and the strong Jovian magnetosphere.

1.2. JUICE/MAJIS instrument and focal plane

Consequently, the next ESA Large mission to explore Jupiter will include MAJIS. MAJIS is a hyperspectral imaging spectrometer working in the VIS-NIR range (0.5–5.54 μm), where numerous mineral and icy species exhibit diagnostic spectral features. This cornerstone instrument, is under IAS/CNES (*Institut d'Astrophysique Spatiale/Centre National d'Etudes Spatiales*) responsibility with strong contributions from IAPS/INAF (*Istituto di Astrofisica e Planetologia Spaziali/Istituto Nazionale di Astrofisica*) and Leonardo company; it is described in (Langevin et al., 2018).

MAJIS works with one telescope and two detectors with their own optical path, each one being Teledyne H1RG with an 18 μm pitch. One will be used for the VISNIR channel in the 0.5–2.35 μm range and the other for the IR channel in the 2.25–5.54 μm range. The IR channel detector (grey box with orange strap on Fig. 1) will be maintained at 80–90 K via a thermal link to a dedicated radiator to allow sufficiently low dark current and noise contributions to work in its IR range, while the entire Optical Head of MAJIS along with the VISNIR detector will be at 140 K. Both detectors feature a Linearly Variable Filter (LVF) in front of them, made of coated sapphire, in order to remove the contributions from the grating at diffraction orders higher than 1. The whole spacecraft is partly shielded from radiations by several millimetres of aluminium, which is taken into account in the environmental simulations used to design the tests described hereafter.

Fig. 1. MAJIS opto-mechanic design drawn by Leonardo Company (project communication): the two grey blocks at the end of the optical paths are the FPAs (Focal Plane Arrays), the infrared one is linked by its thermal strap in orange to be maintained at 85 K, while the rest of the Optical Head will be nominally at 140 K. (For interpretation of the references to color in this figure legend, the reader is referred to the Web version of this article.)

To deliver down to Earth its final data in the form of 3 dimensions hyperspectral cubes, MAJIS will acquire series of frames, each one featuring a 400 binned pixels (36 μm pitch) spatial dimension along the slit and a 508 binned pixels spectral dimension along the dispersion direction of the grating. Then, the movement of the spacecraft, adjusted by the rotating mirror in MAJIS telescope, will allow reconstruction of the missing second spatial dimension. All image acquisitions will be split into several sub-integrations due to post-processing requirements that we will discuss later, among which only part of the data will be downloaded to Earth. This critical procedure will be performed on-board by the Main Electronics (ME) to reduce the telemetry need, since only 50 kbits/s are planned to be available so far (project communication).

During its nominal mission, from January 2030 to June 2033, MAJIS will study Jupiter, especially its hot spots and auroral emission as well as performing limb observations of star occultations through the atmosphere. The two close flybys of Europa will take place during this Jupiter orbit period, limited to such a short time for radiation intensity reasons. The flybys of Ganymede, Callisto, remote sensing of Io and flybys of small ring body yet to be chosen will then take place before the 9-month orbit of Ganymede to study its surface extensively. This Ganymede orbit will provide full coverage of the satellite at $<$ 2.5 km/pixel spatial resolution. Those observations are summarized in Table 1.

1.3. Despiking need in the Jovian system

Despite its major achievements, NIMS performances were highly impaired by radiation damages, which permanently disabled 4 of the 17 photo-diodes and the movements of the grating making the acquired spectra of 13 spectral points instead of 408 (Lopes and Spencer, 2007). Those damages were permanent after only two years of mission. The cause for those damages were primarily high-mass and high-energy accelerated particles, such as protons, trapped in the Jovian magnetosphere and capable of forming permanent electronic defects. Transient signal caused by particles such as electrons transferring energy to the photo-sensitive layer of detectors was also an issue on the SSI 2D camera on Galileo.

This highlights one of the most challenging points for this mission will be the radiative environment: radiations in the intense Jovian magnetosphere are extremely hazardous for electronic material and may result either in permanent damages or in transient signal, which is added energy to the photo-sensitive layer of the detectors. These transient signals will be called "spikes" hereafter. In this paper we will focus on this last type of radiation-induced effect, the transient signal. Its criticity is best shown by the high-energy electrons flux expected to reach 3 e−/pix/s, assuming 10 mm Al equivalent shielding, at the closest point to Europa in the current mission definition (ESA and J. Team, 2015), resulting in multiple spike hits, adding noise to the scientific data and impeding their interpretation. It is currently believed (Kollmann et al., 2018) that the

Table 1
JUICE mission targets and foreseen observations at their closest approach. During the long Jupiter orbit, both the satellites flybys and Jupiter's atmosphere study will take place.

Target	Observations	Distance
Jupiter	2.5 years orbit	600 000 km
Io	remote	430 000 km
Europa	2 flybys	380 km
Ganymede	12 flybys and 9-month orbit	500 km
Callisto	13 flybys	140 km
Small ring body	2 flybys	$>$ 600 000 km

main process to accelerate those electrons around Jupiter is adiabatic heating occurring via radial diffusion. The foreseen fluxes of electrons, modelled by IAPS/INAF, to be encountered by MAJIS through the whole mission are illustrated on Fig. 2. Those trapped particles in the Jovian magnetosphere come not only from the solar wind but also from the Jovian plasma torus, mainly fuelled by Io's volcanism (Bagenal et al., 2006). The fluxes given here per pixel for a certain energy range are computed from the simulated flux per square centimeters using the appropriate detector's pixel pitch.

If the spikes were not handled, they would create fake features in spectra which might be mistaken for an expected atmospheric emission, or it would raise the level of an absorption band characteristic of a chemical compound on the surfaces, possibly making it undetectable or simply unidentifiable since its shape would not match the spectral models anymore. Those potential deformations are illustrated by Fig. 3 on spectra of Ganymede acquired by NIMS (McCord et al., 1998). It may even make the information lost at some spatial or spectral positions by saturating the pixels (such as for Galileo/SSI (Klaasen et al., 1997)). Considering the spike rate given above for the worst case at Europa (3 e−/pix/s), and the fact that those electrons will create spikes of various intensities, they will even change the continuum of the spectra and create fake spectral bands. Those problems have been encountered by the NIMS instrument as described by (Hibbitts et al., 2000), where the identified spikes are described as positive or negative anomalous signal ranging from a few DN to tens of DN (Digital Numbers).

1.4. Spikes formation mechanisms in HgCdTe

Given the incident distribution of electrons shown in Fig. 2, some of these electrons (those with a high penetration depth) will cross the shielding material and simply reach the FPA (Focal Plane Array) with an almost unchanged energy (Raftari et al., 2018), while some other electrons will loose some of their energy in the shielding material and generate secondary electrons (Pickel et al., 2005). The FPA consists of an HgCdTe layer, which has been grown on a removed CdZnTe substrate (see (Beletic et al., 2008)), linked to its Si ReadOut Integrated Circuit (ROIC) by In bump bonds. During the integration time, each pixel in the HgCdTe layer has a high-field depletion area near the In bonds and a low-field diffusion area elsewhere, which allow for charge creation when a photon from the science targets hits the detector. However, when an energetic primary or secondary electron from the environment reaches

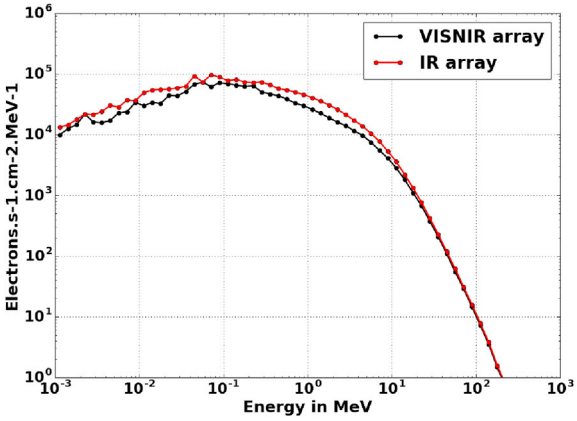

Fig. 2. Energetic distribution of electron flux in $e-/cm^2/s/MeV$ seen in average by each detector on VISNIR and IR channel, simulated for in-flight conditions taking all shielding into account. Simulation has been done by IAPS/INAF, differences between channels come from different mechanical housings resulting in different shielding environments. There will be no electrons above 100 MeV and most of their population will be below 10 MeV with a distribution peak at 100 keV, therefore we tested the detectors with ~ MeV and below β^- radiation sources.

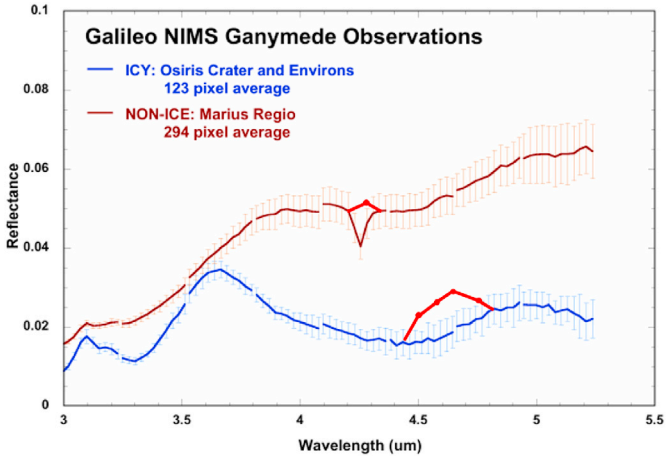

Fig. 3. Sample of infrared spectra obtained by Galileo/NIMS (McCord et al., 1998), on the surface of Ganymede at several places. Spectral signatures evolve with the position showing water ice regions. The added red dots illustrate the possible effects of electrons transient signal. (For interpretation of the references to color in this figure legend, the reader is referred to the Web version of this article.)

this FPA, it will also generate charges along its path if its penetration depth is not too high, either in the depletion area which will be counted by the ROIC as additional signal in the hit pixel, or in the diffusion area in which case it may diffuse from the hit pixel to contiguous ones and be finally counted in another depletion area (see (Pickel et al., 2005)). This means that single electrons may generate several spikes in the shape of a cluster, especially if the incidence angle is high (Becker et al., 2005). On the other hand, some electrons with high energies may also yield little to no energy while crossing the detector ((Cosslett and Thomas, 1964) or (Kanaya and Okayama, 1972)).

Then, once an electron has reached a pixel and is interacting with it, the rate of charge generation in the pixel's depletion and diffusion areas depends on the ionization rate of the HgCdTe layer and on the Linear Energy Transfer (LET) of the electron. First, the ionization rate is estimated using the rule of thumb given by (McCullough, 2009) to consider that this energy is 3 times that of the cut-off wavelength, meaning ~ 0.7 eV for our 5.54 μm cut-off. Then, the LET of electrons of energies ~1 MeV passing through HgCdTe alloy is given to be 250 eV/μm by (McCullough, 2009), which is for comparison one order of magnitude lower than proton's LET in HgCdTe, since LET decreases with the mass of the incident particle (L'Annunziata, 2012). LET will also vary with incident energy, it increases when the electron's energy decreases (Taylor, 1970), meaning that it will have a distribution of values as the incident population of electrons has one. At last, we need to estimate the thickness of the HgCdTe crossed layer to compute the expected number of charges created and not just their rate. A rule of thumb given by (Beletic et al., 2008) is that the thickness must be at least equal or superior to the cut-off wavelength, for simplicity we will consider 10 μm for both detectors studied here, yet it may vary because of the very high mobility of the electrons. We obtain an estimated average of 3500 radiation-induced charges for each electron along all its path, which should be the order of magnitude of the spikes level in the images.

The sum of those charges, either photon- or electron-induced, are turned into Digital Numbers (DN) at the end of the integration time by the ADC (Analog-to-Digital Converter) of the PE (Proximity Electronics) which feeds the spacecraft onboard memory. As we see, the spike's average energy is rather low and not likely to saturate the pixel's quantum well, so it may just be adding signal to the photon-induced one, creating the potential misinterpretations we saw in the previous paragraph. To sort those two contributions out the foreseen strategy is time filtering as detailed in the next paragraph.

1.5. Foreseen despiking strategy

Knowing this, we plan to develop the following time filtering algorithm, which needs to be simple and memory-cheap since it will be implemented on-board the spacecraft with limited resources.

This in-flight despiking algorithm has two tunable parameters: each integration of a pixel will be split in several sub-integrations (M parameter, typically between 10 and 20) of a few hundreds of milliseconds. Then, the values of the pixel for each sub-integration are sorted out in increasing order. Only the few lower values (N parameter, typically between 1 and 5) are kept as unspiked values and summed to result in the final pixel value for this integration which will be sent by the spacecraft as an image. The expected performance for the filtered images after the algorithm is less than 1% of the pixels still containing a spiked value, with M and N parameters being adapted according to the expected radiative environment at each phase of the mission, to fulfil this objective while maintaining sufficient SNR (Signal to Noise Ratio) for science targets.

However, we can see that this approach entirely relies on the assumption that the lowest values of the pixel will always correspond to the absence of electron impact. As we saw in the previous paragraph, this may be wrong in some situations, which are:

1. If some spikes have such energy levels that they saturate the pixel, it may cause additional blooming;
2. If a single electron hit spreads its energy to adjacent pixels forming a cluster of spikes, with the average level of a neighbouring pixel being higher because of the target's signal, this value might be still counted in the lowest occurrences of the neighbour pixel yet it contains a spike;
3. If some spikes create persistence over time in the pixel, we may end up without any unspiked frames;
4. If the surrounding materials in the focal plane, such as the sapphire substrate of the LVF or the anti-reflection coating on the detector, generate more secondary electrons (*glow*) than modelled by ESA it would worsen the situation and the initial guess of despiking parameters M and N would become wrong;

Therefore, in order to ensure that the algorithm will work properly in flight conditions and to obtain a first estimate of the M and N parameters, we need to perform tests on candidate detectors with radioactive sources of electrons. The previous points will be our main analysis goals after measurement campaigns, to check for typical spike energy and numbers (point 1), clusters (point 2), persistence (point 3) and glow (point 4).

2. Experimental setup and acquisitions

2.1. Test bench requirements

The expected fluxes during JUICE mission range up to 3 spikes/pixel/s during both Europa flybys, which is the main reason for this limited number of two flybys despite Europa being one of the major science objectives of the mission, but it will be far lower during Ganymede orbit for instance. Therefore the test bench needed to reproduce all of these conditions had to feature several radioactive sources allowing for simulation of several mission phases with various energy distributions and various activities. The electron fluxes from each source must be calibrated right before the test, while the detector under test must be maintained under cold and vacuum conditions. The order of magnitude of temperature for ROIC electronics are the temperature of liquid Nitrogen (> 77 K) and the pressures are $\sim 10^{-7}$ mbar. The actual temperature of the detector chip must be known at any moment to ensure a suitable dark correction of the images, which is made possible by PT100 probes attached to the Copper detector's holder.

2.2. CSL setup description

The setup fulfilling the requirements for these tests has been developed at CSL (*Centre Spatial de Liege*) specifically for JUICE purposes, it is illustrated on Fig. 4 and extensively described by (Carapelle et al., 2019). We rely on a reference spectrometer under vacuum which yields the energetic distribution of electrons generated by 3 β^- radioactive sources: Ruthenium 106, Strontium 89/Yttrium 90 and Chlorine 36. Then a motorized source wheel brings the sources in front of the MAJIS cryostat where the detector is irradiated at several operating temperatures and integration times. The cryostat is closed by a specific window which is transparent to electrons but not to photons in order to irradiate the detector while maintaining it in dark conditions. The distance between the sources at the edge of this motorized wheel and the detector chip itself was 8.27 mm during the first campaign in 2016 and 7.07 mm during the second campaign in 2018. The energetic spectra of the three sources measured by CSL spectrometer are given on Fig. 5, with MAJIS cold plate and electron-transparent window placed in the spectrometer in the same way as in the detector's cryostat. Therefore, the measured fluxes should account for most of the generated secondary electrons but not all of them since the environment encountered by the primaries is not the exact same one as in the test cryostat. The small flux differences between sources used for September 2016 campaign and for June 2018 campaign come from radioactive decay and a slightly different energy bin used for measurements: 0.58 keV for September 2016 and 0.56 keV for June 2018.

The Ru and Cl sources have the same activity, namely 37 kBq, with energy distributions peaking respectively at 0.6 and 0.2 MeV, while the Sr/Y source has a lower 3.7 kBq activity with an energy distribution peaking close to the Ru at 0.5 MeV. For Cl, due to its low energy/shallow penetration depth, its resulting distribution after MAJIS window and cold plate yields four times less electrons than Ru despite having the same activity. As for Ru, its short half-life (1.02 years) made the use of a fresh source mandatory for each campaign and its radioactive decrease was taken into account in source reference measurements so that Fig. 5 gives the actual fluxes at the time of the tests on both detectors. All sources have been imaged in long series of frames at short integration times

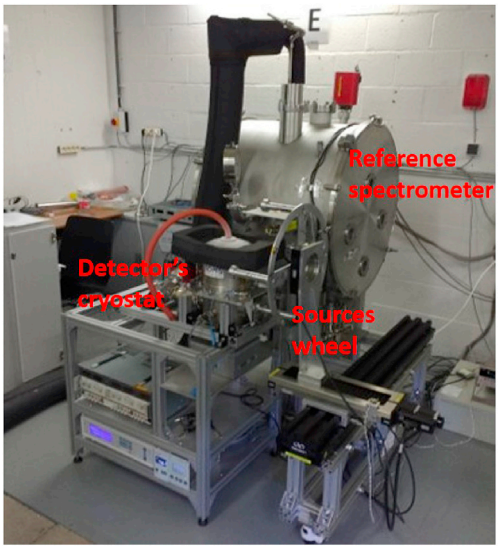

Fig. 4. CSL test setup: at the front centre the three sources are mounted at the edges of the motorized wheel, while the detector's cryostat is on the left (with its orange pipe) on its monitoring rack, and the tank at the back contains the CSL electron spectrometer to characterize the actual sources flux. (For interpretation of the references to color in this figure legend, the reader is referred to the Web version of this article.)

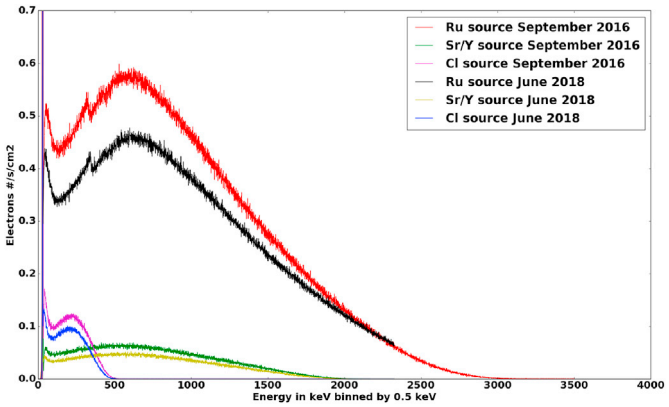

Fig. 5. Energy spectra of the three sources, obtained by the CSL spectrometer, after MAJIS representative cold plate and window shielding taken into account. The sources were at different distances during the two campaigns and the freshness of sources were different.

(between 100 ms and 1s) that can be summed on ~ 4000 frames to reproduce the Europa phase electron fluxes out of the actual fluxes of those sources which do not exceed 0.004 e−/s/pixel. It appears that none of the sources exceeds 3 MeV which is well below the highest energies expected in flight according to Fig. 2, for two reasons: one being that the procurement of more energetic sources was difficult and raised security issues with the planned setup at CSL, the other one being that we assumed that the higher energy electrons would not deposit enough energy in the detector to be of concern. This last aspect will be confirmed by our measurements in the following paragraphs.

2.3. Tested detectors

2.3.1. The Sofradir Retina

The first tested detector is a Sofradir Retina NGP, which was a candidate in the selection process of MAJIS detectors. It is read by a custom ROIC (*ReadOut Integrated Circuit*) of CTIA type, n on p doped, made of an MCT layer deposited on CdZnTe via Liquid Phase Epitaxy (LPE) as explained by (Chorier et al., 2001). The substrate is then removed. Its cut-off wavelength is 5.3 μm and it has a Full Well Capacity (FWC) of ~ 740 000 e−. In terms of dimensions, it is a 1024 × 1024 pixel array, with a 15 μm pitch, which are expected to be binned in flight. Its thickness is not precisely known since it is not given by the manufacturer, we assumed for simplicity that the order of magnitude of 10 μm determined in section 1.4 using the rule-of-thumb given by (Beletic et al., 2008) (given for HxRG detectors) is also applicable to this detector. This is questionable considering the manufacturing differences between both detectors, but will not be of consequences for the interpretation of the results presented here. We measured its Readout Noise at around 250 e−per single read at nominal operating temperatures of 80–90 K.

During the test, we added a custom filter holder in aluminium to accommodate a small sample of the Linear Variable Filter (LVF) which will be in front of the detector during the mission to discard the contributions of higher orders of diffraction. For those tests, only the sapphire substrate of the LVF was used since it is the part that might generate glow - secondary photons - after being hit by an electron. The sapphire and its holder covered about a quarter of the detector's area, generating a geometry where some of the electrons cross only Al before reaching the photo-sensitive layer while only a small fraction do cross the sapphire substrate as intended.

2.3.2. The H1RG engineering grade

The future flight detectors for MAJIS will be Teledyne H1RGs with its ROIC being a source-follower (SFD) type. Fig. 6 shows the cryostat setup with the detector behind a cold plate to shield it from light. It also

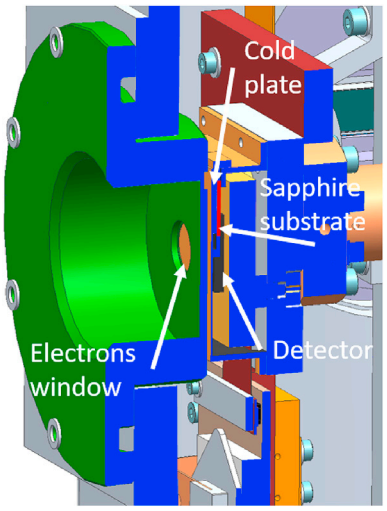

Fig. 6. Side view of the H1RG detector in its cryostat used for electron tests. The green part is the outside flange of the cryostat where the electron sources can be placed, then the electrons go through an electron-transparent window. They encounter the cold plate which surrounds the detector protecting it from light which alters the initial distribution of electrons, and at last some of them cross the sapphire substrate part (in red) before reaching the detector itself (black part). (For interpretation of the references to color in this figure legend, the reader is referred to the Web version of this article.)

consists of an HgCdTe layer deposited on CdZnTe substrate which is later removed, but via Molecular Beam Epitaxy process. Its doping is p on n unlike the Sofradir, but it has the same cut-off wavelength of 5.3 μm. Its FWC is shallow at 80 000 e− and the flight model is expected at 60 000 e−. The reverse bias voltage used by Teledyne in this case is 256 mV. Its dimensions are 1024 × 1024 pixels and an 18 μm pitch, also supposed to be binned once in flight yielding a pixel definition of 36 μm. As for the Sofradir one, the exact thickness of its photo-sensitive layer was not provided by the manufacturer.

It can be read in two modes, called Slow and Fast, which have both been implemented using a dedicated microcode developped at IAS. The Slow mode works in Correlated Double Sampling (CDS) and allows for integration times longer than ~ 700 ms, it will be one of the modes actually implemented in flight and is extensively used in the analysis presented here. This CDS is performed with one reset image (1) and one read (2), separated by the required integration time, after which the two images are subtracted (2–1). The Fast mode works with a single read-reset and allows for integration times longer than ~ 60 ms, therefore it will be used in this analysis for the study of persistence which requires short delays between integrations, yet its poor performances will not allow its use in flight where it will be replaced by another mode that was not implemented at the time of the tests, therefore it will not be extensively discussed here. Fast mode images being single read-reset they mandatorily require the acquisition of series of dark conditions images that will be subtracted from the single read-reset images.

For the electron tests it also featured a part of sapphire filter substrate in front of the detector chip but actually covering less than a quarter of it. This substrate was held by its sides thanks to the cold plate carved in a drawer shape, it is 1 mm thick with 1 mm remaining between its bottom surface and the detector, representative of the flight model.

2.4. Measurement campaigns

The first test campaign was conducted at CSL in Belgium on Sept 20–22 2016 with the Sofradir detector in its cryostat. Our test plan included several measurements without sources in front of the detector to get "dark" reference frames as well as measurements at three different detector's temperatures since it affects dark current and RON (ReadOut

Noise) values: 80, 85 and 90 K. All detector's temperatures were measured by the regulating cold finger at the rear of the detector's Cu base plate, we estimated the offset with the actual detector's temperature to be about 1 K hotter. We tested the shortest and longest foreseen integration times during the mission (110 μs and 10 s) while focusing our acquisitions on typical in-flight integration times: 100 ms and 1 s. We took more than 10 000 frames accounting for 40 GB of data during the test, for all integration times, detector's temperatures and sources (Ru, Sr/Y, Cl and no-source).

A similar procedure took place on June 5–6 2018 with the H1RG engineering grade detector in its cryostat. The range of integration times was more limited due to the shallower Full Well Capacity and the readout speed, for this reason most of the measurements were taken at 100 ms in Fast mode and 800 ms in Slow mode, which are also representative of the typical sub-integration times in flight. Part of the data were processed on the fly to adapt our acquisitions and integration times to the results. We measured independently the dark current and RON for each mode before irradiation.

3. Data analysis methods

3.1. Measured parameters

To assess the behaviour of our detectors during exposure to the electrons, we wanted to measure the following parameters:

1. Spikes counts and energy spectra
2. Clusters number and size
3. Signal persistence over time
4. Potential glow from surrounding materials

Data are acquired in bursts of 32 frames, which is imposed by the communication software for the H1RG and series of 64 frames for the Sofradir. A sample frame from H1RG is shown on Fig. 7, where we summed a series of 31 frames at 800 ms exposure each, to obtain sufficient spikes flux for visual representation. The color of pixels codes the intensity of the signal, expressed in Digital Numbers, the maximum being 65535 DN for Sofradir and for Slow mode with H1RG since the values are coded on 16 bits, while it is 4096 DN for Fast mode since the values are coded on 12 bits, though the actual saturation of a pixel usually occurs at lower levels than the maximum numerical value. The centre of the source is easily identified by the density of spikes, as well as the angle spread effect.

We always handled these data as time series since it is impossible to distinguish a spike from a Random Telegraphic Signal (RTS) on a single

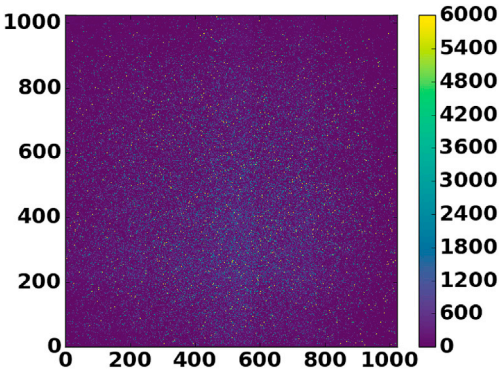

Fig. 7. Image resulting from the sum of 31 integrations of 800 ms each taken by the H1RG detector protected from any light signal by a cold plate but with the Ru source in front of the cryostat. The observed spikes energies expressed in DN are color-coded, their spatial distribution shows that the source was not perfectly centred. (For interpretation of the references to color in this figure legend, the reader is referred to the Web version of this article.)

frame. Therefore, we grouped the frames in series of 32 for each source at each integration time, as well as dark frames where the sources were not in front of the detector to be used as a reference. The first image of the series is always discarded as it is garbled. The series of 31 remaining dark frames are used to create a bad pixels map, by flagging all pixels exhibiting a standard deviation three times above the median standard deviation of the whole array. These bad pixels will not be taken into account by the spikes detection algorithm, they represent 7% of the array for Sofradir and 4% for H1RG in average as we found in our data.

The definition of cluster of spikes that we will use is a group of pixels having one contiguous side (not in diagonal) which are all impacted by a spike on the same frame in the time series. The energy or intensity of the spikes are defined here as the level of the pixel at the frame were a spike is detected, either in DN or in charges, relatively to the median level of this pixel computed on the rest of the time series; therefore it is the added signal of the spike.

The spikes detection algorithm is then applied to these time series, as well as the dark one to measure the amount of fake positive detections. The steps of the algorithm are detailed in the next paragraph, it is used to count spikes, measure their relative energy, angle from the centre of the source, keep track of their spatial and time positions, count clusters and measure their size.

3.2. Spikes detection algorithm for analysis

A dedicated spikes detection algorithm proved mandatory for this analysis since the need to retrieve both the energy and position of each spike to understand their behaviour is very different (and more processor and memory demanding) from the need to blindly remove them once in flight. This question is well-known for cosmic rays, for which similar algorithms have been developped such as Offenberg et al., 1999, though we added more steps here to account for some erratic behaviours of our detectors that might be confused with spikes. The focus of this algorithm is the identification of the properties of the spikes relatively to the normal behaviour of the detectors. This algorithm works on data described in the previous paragraph and follows these steps:

1. Find the maximum value in each pixel's time series
2. Compute median value and standard deviation on the time series ignoring this maximum value
3. Check that the maximum is above median +3 standard deviation
4. Check that the standard deviation of the three values before or after the maximum have a standard deviation below the average one
5. Check that the series without the maximum is below 30% of this maximum
6. Then the maximum is considered as a spike and its position, energy and angle from the source is stored
7. This process is repeated once on the series from which the first identified spike has been removed to look for potential second hit

The assumptions motivating this algorithm are: that all pixels not flagged as bad might be impacted by a spike, the candidate is the maximum (step 1) and it has to be significant with a 3 sigma criterion (step 3) and the surroundings of the spike has to be flat enough not to mistake it with RTS (step 4). With the algorithm stopping at step 4, we encountered results that were highly polluted by fake spikes (almost half of the detections in some cases) and a very poor completeness of the detection at low energies which would have distorted the retrieved energy distributions. Therefore, we needed a criterion of *well-behaving* pixel that would also depend on the spike-candidate energy (the lower the energy, the more compelling the criterion), which is why we added step 5. The 30% has been arbitrarily determined during the validation of the algorithm (see next section) with simulated spikes in order to find the value guaranteeing the best compromise between completeness of the detection and amount of fake detections. At last, step 7 allows for detection of a potential second spike on the same pixel, since the

probability of a third hit is very low (< 1% even with Ru source) it is ignored.

The tuning and performances evaluation of this algorithm are detailed in the next validation paragraph, in average we obtained ~ 70% of completeness (true spikes retrieval) and less than 1000 fake detections. Of course it is impossible to guarantee on real data that none of the detected spikes come from natural radioactive source, since they are undistinguishable.

3.3. Algorithm validation

In order to validate the performances of this algorithm and determine the arbitrary scale value, we used time series obtained during the test campaigns as reference data, meaning without any radiation source in front of the detector. We added spikes at spatial and time positions that were randomly determined at each run, with one spike every 1 DN on each frame of the series, yielding 31 injected spikes that should be detected in total at each energy if we histogram the results with a 1 DN bin. We tested various values for the highest energy injected, up to 10 000 DN.

Fig. 8 shows the amount of missed spikes for two dark frames of the Sofradir detector at 80 and 90 K respectively. Here, we used the final optimised arbitrary factor of 30% for step 5 of the algorithm. An ideal algorithm would yield a perfectly flat line centred on 0, yet here we miss about 30% of the spikes as we can see on the plot, with almost no dependence on the energy when it is higher than ~ 200 DN.

At low energies, other phenomena are observed: below 20 DN, no spike is detected on any detector. This threshold effect will introduce differences with the incident electrons measured distributions, yet it was inevitable since a very low spike is indistinguishable from dark erratic behaviour, and our aim is to analyse only spikes induced by electrons so as to obtain reliable information on the effect of electrons. Between 20 and 200 DN, the amount of detected spikes suddenly increases and even goes above the amount of injected spikes (below 0%) for the 90 K conditions. This is actually where most fake spikes (not injected by our simulation) are happening because of the noise levels. We have reached a number of fake detections always below 1000, typically 500 but slightly varying with detector's temperature and between H1RG and Sofradir. The amount of fake spikes increases at 90 K since temperature increases the dark current level and noise. This will make interpretation of energy distributions at these levels difficult and to be taken with caution.

The validation of this algorithm allows for a correction factor to be applied to the total counts we will obtain when analysing real data: the correction factor is determined by the completeness evaluation of our detection algorithm, which yields a factor of 1.34 for H1RG counts corrections and 1.37 for Sofradir counts corrections. These factors take into account the percentage of pixels that are flagged as bad in the very first steps of data processing (4% for the H1RG and 7% for the Sofradir) and the amount of missed spikes in the simulations (30%). Though 30% seems unsatisfying, we had to make a trade-off for this completeness, since a less severe detection algorithm would have detected way more fake spikes that would skew our sample. This effect is illustrated by Fig. 9 where the increase of false positives with threshold is steep while false negatives are little sensitive to it. Therefore we chose 30% as the higher threshold that kept the amount of false positives to the minimum. We considered the addition of false positives more impairing for our study than missing real spikes, as long as their distribution is not distorted by a selection effect. Since the position and energies of missed spikes can't be guessed, all plots of parameters linked to the detected spikes in the next sections will be done using only the detected spikes without any simulated addition, as for the total number of spikes it can be computed from the detected ones using the above mentionned correction factors. Lastly, the amount of fake spikes detected being always of a few thousands, we fixed the precision of all counts that will be given in the analysis to $1.0\ 10^3$.

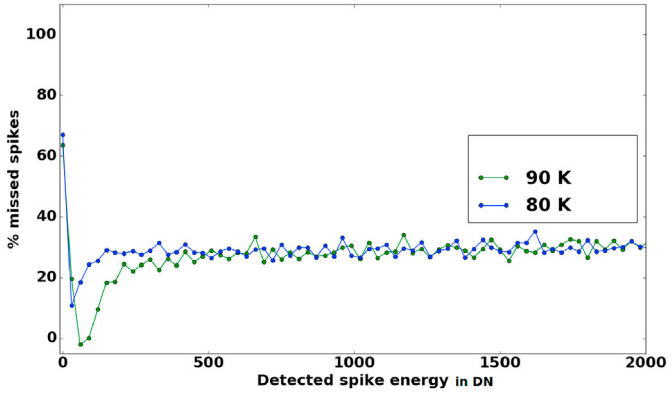

Fig. 8. Difference between expected detections per 30 DN bin and actual detections using the optimised parameters of the algorithm in percents. The blue curve is obtained using Sofradir dark frames at 80 K while the green one is obtained also with Sofradir at 90 K. We observe an increase of fake detections at low levels especially at 90 K since the dark noise is higher, and a threshold effect at very low energy. The situation is similar for H1RG. (For interpretation of the references to color in this figure legend, the reader is referred to the Web version of this article.)

4. Results and interpretation

4.1. Spikes counts and energy distributions

Figs. 10 and 11 give the histogram of retrieved energy distributions of spikes in terms of flux and probability respectively. The red, green and magenta curves are for the Sofradir, while the black, yellow and blue ones are for the H1RG in Slow mode. The energies have been converted from DN to physically meaningful electrons (or charges) using the ADC gain of each detector to make the result comparable between both detectors and with the prediction of deposited energy we made in paragraph 1.4. This gain is 5 e−/DN for H1RG in SLOW mode and 80 e−/DN in FAST mode, while it is 45 e−/DN for Sofradir, which required a rebinning (by 50 e−) of the curves for their comparability.

The integral of the curves plotted on Fig. 10 are given in the third column of Table 2, which is the total amount of detected spikes, to be compared to the second column of this Table which gives the measured amount of electrons sent from the sources. Therefore, the integral of these histograms show that no major difference between electrons and spikes appear: both counts are of the same order of magnitude. We also

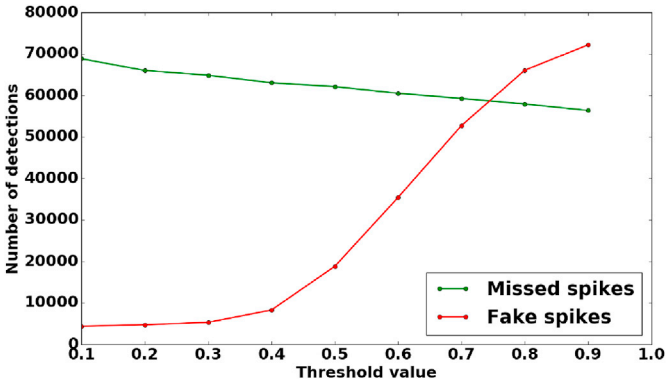

Fig. 9. Evolution of the false positive detections (fake spikes in red) and false negatives (missed spikes in green) versus the threshold value of the algorithm. This threshold corresponds to step 5 in the algorithm description where 30% is given: here we explore values from 10% to 90%. (For interpretation of the references to color in this figure legend, the reader is referred to the Web version of this article.)

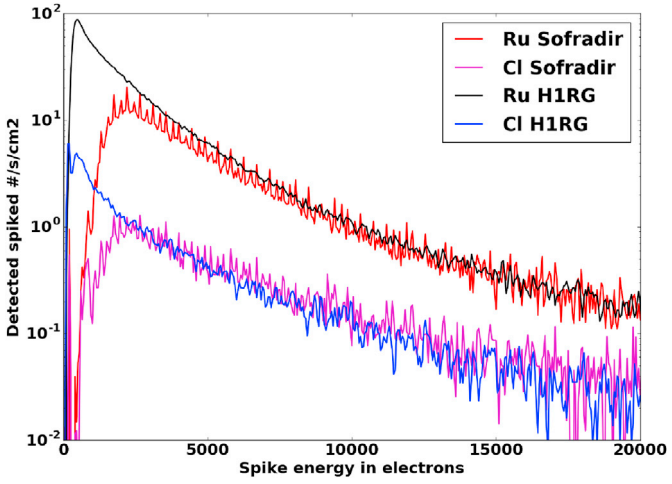

Fig. 10. Detected fluxes of spikes per second and cm2 versus their energy, in vertical log scale, for both detectors and the two most different sources: Ru and Cl. Red and magenta histograms are for the Sofradir with sources Ru and Cl respectively, while black and blue histograms are for the H1RG in Slow mode with Ru and Cl respectively. Data are binned by 50 e−. (For interpretation of the references to color in this figure legend, the reader is referred to the Web version of this article.)

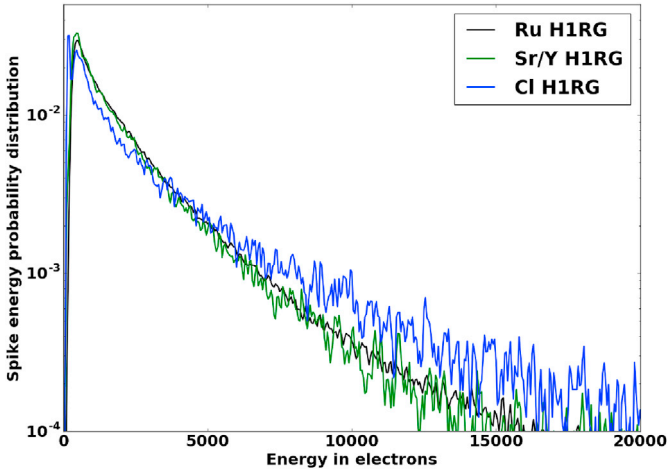

Fig. 11. Measured energy deposition probability per spike, in vertical log scale, for the H1RG with the three sources in Slow mode. Black, yellow and blue histograms are for Ru, Sr/Y and Cl sources respectively. Data are binned by 50 e−. (For interpretation of the references to color in this figure legend, the reader is referred to the Web version of this article.)

check on this Fig. 10 compared to Fig. 5 that when the flux of incident electrons increases (Ru compared to Cl here), it also increases the flux of spikes. Yet, differences of shape are very marked: the difference of low-energy cut-off between H1RG and Sofradir on Fig. 10 is a consequence of both the detection algorithm and the detector's sensitivity. Indeed, we set the threshold of our detection at 20 DN in our previous section 3.3, which translates into 100 electrons for H1RG and 900 electrons for Sofradir given their respective gain, explaining in part the cut-off that we observe. In addition, the Sofradir detector is also intrinsically less sensitive than the H1RG which also contributes to the decreasing shape of the observed distribution at low energies.

The measured average energy on these curves are close to the predicted value of ~ 3500 e−in part 1.4: we find 2700 e− and 3600 e−for H1RG with Ru and Cl respectively, while Sofradir yields 5500 e− and 7200 e−for Ru and Cl respectively. Since these values are expected to vary for different path length and varying LET (depending on particle

Table 2
Spikes detections statistics: detector and source are given in the first column, the second column gives the amount of electrons measured by the reference spectrometer, the third gives the detected amount of spikes, the fourth is the ratio between the two previous columns, the fifth is the number of hits (clusters counted as one) which is expected to be the amount of interacting electrons, and the last gives the average size of a hit (ratio of third and fifth columns). All these values are evaluated on series of 31 frames. The uncertainties on counts are ±1000.

Measurement conditions and sources	Sources electron counts	Detected spike counts	Ratio spikes/ electrons	Nb hits (clusters + singles)	Average hit sizes
H1RG Ru 85 K 800 ms	100 000	248 000	2.5	141 000	1.8
H1RG Sr/Y 85 K 800 ms	8000	27 000	3.3	12 000	2.2
H1RG Cl 85 K 800 ms	5000	16 000	3.2	7000	2.3
Sofradir Ru 85 K 1 s	104 000	77 000	0.7	63 000	1.2
Sofradir Sr/Y 85 K 1 s	10 000	12 000	1.2	10 000	1.2
Sofradir Cl 85 K 1 s	5000	8000	1.6	7000	1.3

Table 3
Summary of despiking algorithm performances on dataset acquired at CSL with an equivalent flux of 1.2 spikes/s/pix. M is the number of sub-integrations at 100 ms integration time which are sorted in increasing order, while N is the number of frames that we keep as unspiked values.

M	N	% remaining spikes
3	1	2.4%
4	1	1.1%
5	1	0.3%

energy) these disparities were expected. However, the ranking of these average energies shows that the least energetic source (Cl) yields more energy in the form of spikes to the detector than the most energetic source (Ru). This is better illustrated and explained by Fig. 11 where the previous histograms are normalized to their integral, giving an energy probability for one spike coming from each source (here on the H1RG detector, the situation is similar on Sofradir). On this Figure, we check that the least energetic source Cl (blue curve) has a higher probability of forming bigger spikes than Ru or Sr/Y sources (black and green curves), which have very similar energy distributions: the source that does not produce electrons higher than 500 keV according to Fig. 5 generates more spikes than Ru and Sr/Y starting at an energy of about 4500 e−. This observation is explained by the fact that a least energetic incident particle will have a higher LET, yielding more energy to the material per length unit, as long as it remains in the range of the total energy available, which is the case here since one electron-hole pair is generated by 0.7 eV in HgCdTe and the sources have typical energies of 10^5 eV.

The other discrepancy in these average energies is between both detectors: for the same source the Sofradir detector always exhibits a higher average energy of spike, while its spike counts (see Table 2) are always lower by a factor of ~ 2–4 than on the H1RG. To account for this effect, we need to consider the formation of clusters of spikes.

4.2. Spatial clustering

An example of clusters of spikes is given by Fig. 12, where the color codes the relative spike level in DN. We observe several single hits, and clusters of 2, 3 or 4 pixels in various shapes. To explain these observations, we have to consider how the electron is releasing energy to the photo-sensitive layer when it crosses it, as explained in the paragraph 1.4, especially that a single electron will yield its energy all along its path and potentially in pixels contiguous to the one it impacted first,

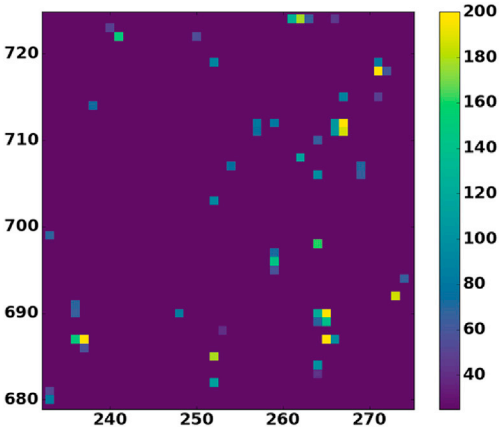

Fig. 12. Zoom on spikes impacts on a frame of the H1RG detector, with the color coding the energy of the detected spikes in DN. (For interpretation of the references to color in this figure legend, the reader is referred to the Web version of this article.)

generating a cluster of spikes. However one electron can only generate a single hit or one cluster at top, but not several clusters, as we assessed in our cases by checking that the clusters in a radius of two pixels around all single hits (which are candidates for multiple-clustering spikes) were not found in numbers higher than what randomness produces.

These random processes can also generate clusters if several electrons happen to hit contiguous pixels randomly. The probability of these stochastic clusters will of course decrease with the size of the considered cluster and with the amount of expected electrons. Therefore, we performed Monte-Carlo simulations with the amount of electrons corresponding to each detector and source we had in order to compare the stochastic clusters formed in these simulations to the measured amount of diffusion clusters in our data. For clusters of 2 pixels we obtain about 10% of stochastic clusters compared to the total amount of clusters of 2 found, and this drops below 1% for clusters of 3. Therefore, we will consider this contribution negligible and assume that clusters are formed via energy diffusion.

On Fig. 13 we plot the same histograms that on Fig. 10 but for Ru source only and in vertical linear scale to allow for a precise comparison: we observe that both distributions exhibit very similar amounts of high-energy spikes, but the H1RG curve has higher amounts of spikes for energies lower than 7000 ~ 8000 e−. Therefore, the fact that Sofradir has higher average spike energies than H1RG might be explained by these clusters: once an electron reaches the H1RG photo-sensitive layer, it will spread its energy more easily than in the Sofradir, generating clusters of lower-energy spikes, which correspond to the population that we observe at energies below 7000 e− on Fig. 13 for the H1RG. This effect appears to be strong, since it overcomes what we would expect from pixel size: the Sofradir pixels being only 15 µm in size which could favour energy diffusion to the neighbouring pixels, while H1RG pixels are 18 µm. It is however supported by the well-known higher cross-talk in the HxRG: usual cross-talk values for Sofradir detectors are below 3% (Fieque et al., 2019), while for H1RG values between 4 and 10% were standard until recent improvements (Prieskorn et al., 2013), which are not implemented in the detector we used though.

Another way to check for this tendency of the H1RG to let the energy spread more easily through pixels, forming more spikes of lower energies, is to plot the histogram of the cluster sizes on both detectors to see their evolution. These histograms are plotted on Fig. 14 for the Ru source and on Fig. 15 for the Cl source, the resulting average cluster size for each measurement condition are given in the sixth column of Table 2. The numbers of clusters are decreasing far more rapidly with increasing cluster size on both Sofradir curves (red and magenta) than on H1RG curves (black and blue) as expected. Yet, a new behaviour is identified on these histograms: the clusters of 4 spikes seem to be favoured on the H1RG, with a relative increase more important for Cl source than for Ru. We checked using Monte-Carlo simulated inputs that this tendency was not an artifact of our detection, which it is not, therefore it appears that the diffusion of energy in the H1RG sensitive layer is especially easy in square groups of 4 pixels. This might be indicating that the energy diffusion from the impacted pixel is happening isotropically which would favour clusters of 2 when the hit is close to the middle of a pixel side, and clusters of 4 when the hit is close to the corner of a pixel.

The fact that the Cl source is producing more of these 4-clusters can be interpreted along with the evolution of average cluster sizes in Table 2: it increases when the average electron source energy decreases. If the cluster size is directly linked to the deposited energy both phenomena are explained since we saw that Cl is yielding more energy than Ru or Sr/Y. On Fig. 16 we plot the correlation between the peak energy in a cluster and the size of this cluster. The red squares with their $\pm 2\sigma$ error bars are the average value for each cluster size. The spread of these energies is extremely wide, making the interpretation difficult. Larger sizes of clusters are not represented on the Figure because of their low significance: the plot is limited to sizes with 30 occurences at least. Overall, we

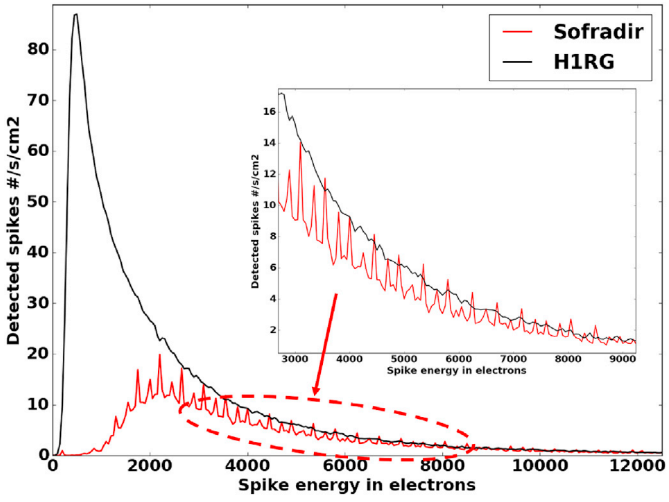

Fig. 13. Histogram of detected flux of spikes, similar to Fig. 10 for the Ru source with both detectors. The vertical scale is linear to allow for more precise comparison of the energy range where both curves start to behave differently, in the zoomed frame.

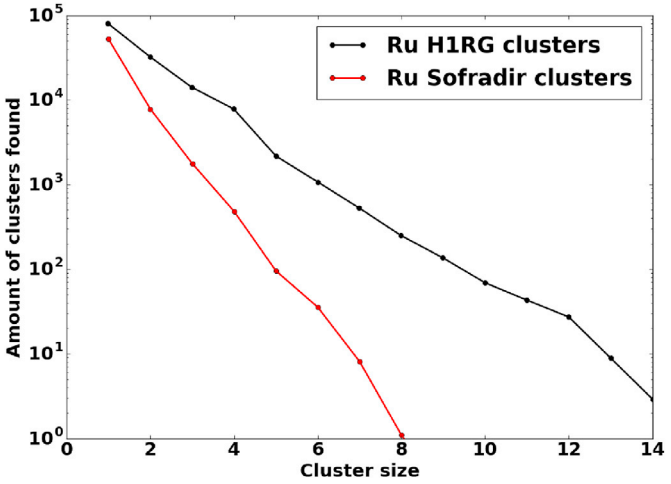

Fig. 14. Histogram of detected clusters versus their size with the Ru source, in black for H1RG and in red for Sofradir. (For interpretation of the references to color in this figure legend, the reader is referred to the Web version of this article.)

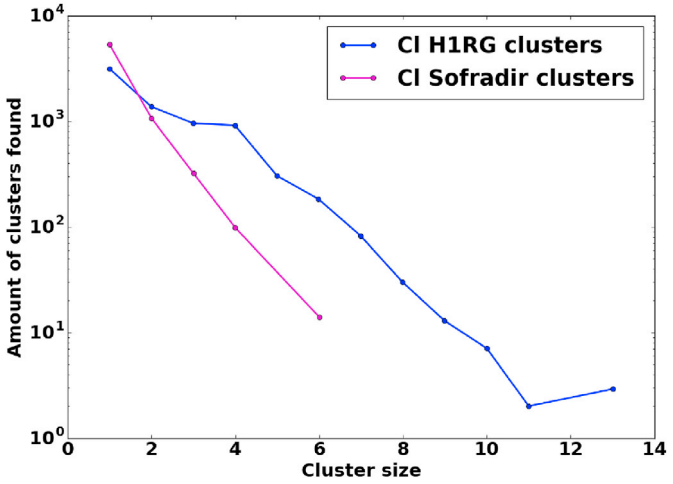

Fig. 15. Histogram of detected clusters versus their size with the Cl source, in blue for the H1RG and in magenta for Sofradir. (For interpretation of the references to color in this figure legend, the reader is referred to the Web version of this article.)

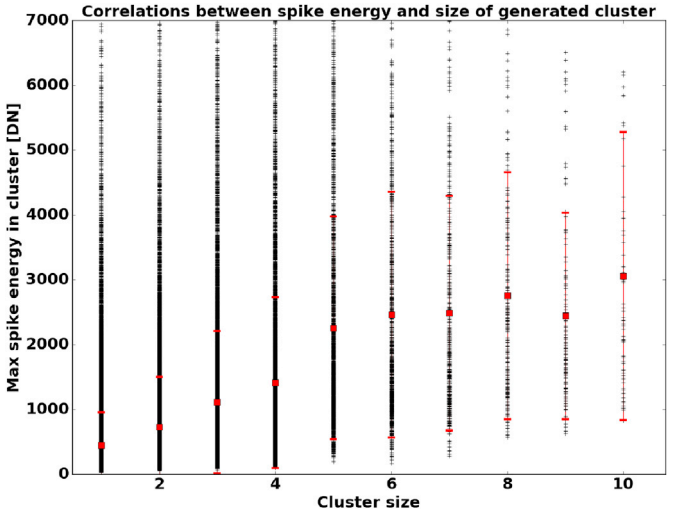

Fig. 16. Correlation between cluster size and peak energy in the cluster for H1RG. The evolution is similar for all other sources. The red squares represent the average value for each cluster size with error bars corresponding to ± 2 standard deviations. (For interpretation of the references to color in this figure legend, the reader is referred to the Web version of this article.)

observe that when the desposited energy is higher, the associated cluster tends to be bigger which is compatible with our assumption. However, giving a slope value for this increase is not relevant for our dataset considering the size of the error bars.

One issue remains in the spike counts even considering this clustering phenomenon, as shown by the fifth column of Table 2: considering that each hit on the detectors (clusters counted as one) is made by an electron from the sources, we still find more electrons than what was measured by the CSL spectrometer (second column) in very similar conditions where the secondary electrons generation should be close. The only set of conditions that is as we expected is with Ru on Sofradir detector where we find less electrons than predicted, since we miss almost a third of the spikes. The excessive total counts of hits in the other datasets might be explained by an underestimated average cluster size (if the other spikes making hidden clusters are too low to be detected), or by a change in our measurement conditions that we did not take into account, such as a change in the source-detector distances. Yet, the origin of this discrepancy is still unclear.

Another point of attention with the clusters concerns the binning of pixels in squares of 2 by 2. Indeed, we must decide whether the despiking algorithm will be implemented on raw data (unbinned, as shown here) or after binning pixels in groups of 4. If an unbinned pixel is impacted by a spike, the whole binned pixel will be affected even if the three other small pixels had no spikes, therefore we would expect that the most favourable scenario is a despiking before binning. However, if each electron forms large clusters in majority, then the tendency might reverse (the two situations being equivalent for sizes of 2) and starting with binning will reduce the relative share of impacted pixels. From Table 2 we see that the average size of clusters for the H1RG flight detector starts at 2 and goes even above for low-energy electrons, which will be numerous around Jupiter, which means that binning before despiking becomes indeed more favourable.

4.3. Persistence

Persistence is expected to depend on the energy deposited in a spike in a simple way: the higher the spike is, the higher the persisting signal is expected and on a longer time scale, since the physical process implied is charge trapping and de-trapping in the semi-conductor layer (see (Serra et al., 2015)). In this respect, the shortest repetition time we tested on both detectors is 100 ms, meaning use of the Fast readout mode as far as the H1RG is concerned. The most energetic spikes we observed on the Sofradir did not generate enough signal to saturate the pixel, because of the high well-depth, while we observed a few saturating spikes on the H1RG. In these conditions, we thought persistence was more likely to be observed on the H1RG detector, because of its shallow FWC and of the SFD readout electronics.

We observed it indeed in H1RG data with the initial version of the Fast microcode (2 cycles of 100 ns allocated for the reset of a line), where there was evidence for a negative persistence (next readout after a spike lower than average) which is especially problematic since our despiking strategy requires sorting values in increasing order. This case is illustrated by Fig. 17 corresponding to a series of 100 ms integration in Fast mode with the Ru source, a large spike at frame 28 (1550 DN) and an anomalous value for the same pixel in frame 29 at −38 DN (−3% of the spike observed in the previous integration). This negative persistence was not expected, a similar effect has been mentionned by Simms, 2010 but only a few pixels away from the centre of signal excess and with different conditions of saturation at longer integration times. The physical behaviour behind our observation remains to be investigated.

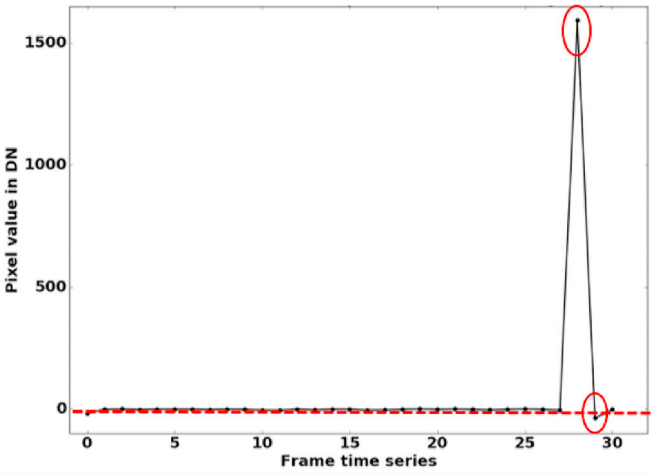

Fig. 17. Time series of one H1RG pixel values with the Ru source in front, showing a spike hit at frame 28 with anti-persistence of 3% of the spike intensity at the next frame 29 with respect to the median of the series. Here the Fast mode is used to allow for a 100 ms integration time at each frame.

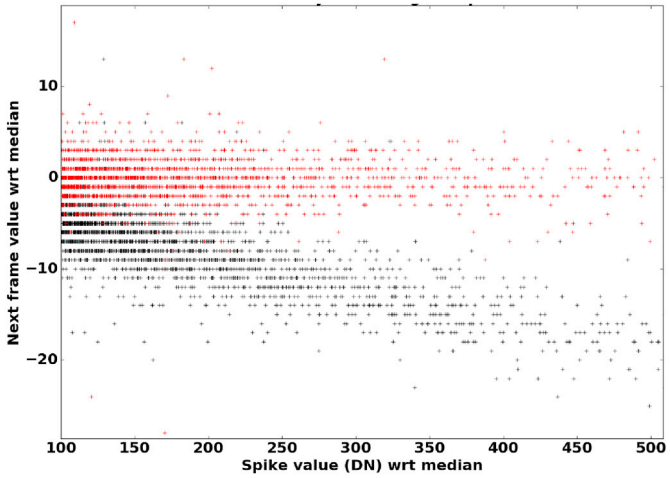

Fig. 18. Correlation between the value of a pixel at the frame following a spike hit versus the energy of this spike in DN, for Fast readout mode frames taken with the H1RG. The black crosses are the resulting correlation with a simple reset, showing negative persistence proportional to the spike energy, while the red crosses are obtained after an increase of the reset time (4 cycles added) showing the absence of detectable persistence within the noise levels. (For interpretation of the references to color in this figure legend, the reader is referred to the Web version of this article.)

In order to systematically check for this effect on all our data, we used correlation plots between the level of pixels in the frame following a spike hit versus the energy of this spike hit. We observed no persistence neither in the Sofradir data even at the shortest integration times (100 ms), nor in the H1RG data acquired in Slow mode at 800 ms integration time. However, the result for H1RG in Fast mode was positive as we said, and this correlation plot is shown on Fig. 18 where the black crosses correspond to the negative persistence we first observed. It shows proportionality to the spike level, with a 3–5% factor, similar to the example of Fig. 17.

During the test campaign, we tested a longer reset (6 cycles) after the readout of each line in Fast mode in order to mitigate this persistence effect. This adjustment of the detector commanding scheme in Fast mode was successful as illustrated by the red crosses on Fig. 18 where no more persistence is detected with the same correlation approach, as shown by the pixel values after a spike centred around 0 relatively to the series of frames instead of decreasing with spike energy before (black crosses). This result gives confidence in the performances of the despiking algorithm.

5. Discussion and conclusions

5.1. Consequences on MAJIS operations and despiking strategy

After checking that all the aspects of the spikes behaviour that might compromise the performances of the foreseen in-flight despiking strategy were not worrying, we used these real-conditions data to check its efficiency. The objective set for this algorithm is 0.25% of remaining spike-impacted pixels (out of the total number of pixels in the array) after one run. As we detailed in paragraph 1.5, the M and N parameters for despiking will be tuned for each situation encountered in flight: considering the dataset we acquired during the H1RG campaign (which is the most relevant case since it will be the flight detector), we were able to reproduce via image stacking an equivalent MAJIS cube of 10 frames simulating a flux of 1.2 spikes/s/pix with sub-frames of 100 ms integration time each.

One of these stacked images is shown on the left panel of Fig. 19. This flux is below the worst case that we will encounter at Europa (> 3 e−/s/pix) but above the most common situations, such as those encountered

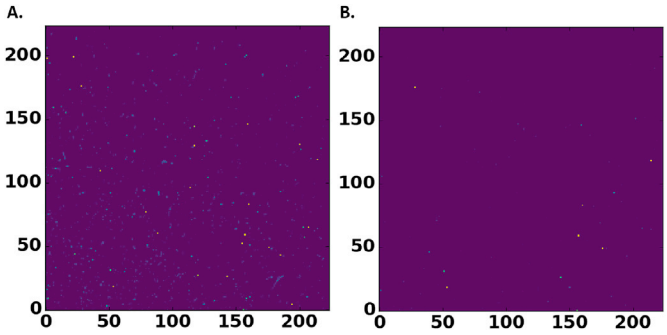

Fig. 19. The left image (panel A) shows a zoom on one of the H1RG stacked images exposed to the equivalent of 1.2 spikes/s/pix, with colors coding the level of energy in each pixel. The right image (panel B) shows the same after application of the despiking algorithm with M = 3 and N = 1, corresponding to more than 2% of remaining spikes according to Table 3. (For interpretation of the references to color in this figure legend, the reader is referred to the Web version of this article.)

while orbiting Ganymede (< 1 e−/s/pix). We applied different strategies to this dataset which are summarized in Table 3, with a starting situation of 12% of impacted pixels on one 100 ms frame considering the simulated rate. A visualization of the result if given by the right panel of Fig. 19.

We almost reach the objective of 0.25% for M = 5 and N = 1 which is a severe sorting situation since only one frame is kept, yet our current observation simulations yield sufficient SNR values (above 10) even in these conditions, which validates the performances of the algorithm on actual data, further consolidating the simulations that had been used so far to prepare this strategy. During the mission, the on-board processing will remain tunable for parameters M and N, as well as the binning which might be different in spatial and spectral dimension, and windowing options to reduce the portion of the array that is actually read resulting in an increase of readout speed. This flexibility, added to the results of this study, validate the despiking strategy for MAJIS.

5.2. Summary of results and interpretation

In this comparative work, we exposed two different detectors, H1RG and Sofradir NGP MWIR, to electron sources of various energies and activities.

Overall, we observe that the number of spikes, or more precisely hits that include clusters of spikes, generated by electrons on the detectors, are of the same order of magnitude as the number of incoming electrons, suggesting that at first order all electrons produce spikes and that there number increases when the source's flux increases. At second order, differences appear, especially in terms of deposited energy which is of the same order of magnitude as what we predicted and increases when the source average energy decreases. This observation is explained by the increasing LET of a lower energy incident particle. Between detectors, the tendency of the H1RG to form clusters of spikes more easily while the Sofradir is very resilient to this effect, explains the larger populations of low energy spikes in the H1RG. This observation is in agreement with the physical separation of pixels in Sofradir but not in H1RG, along with the higher cross-talk in H1RG but is counter-intuitive to what would be expected of the smaller pixel size on Sofradir. We find an average hit size on H1RG of > 2 pixels, while it is slightly above 1 for Sofradir. However, since many similar studies show considerable behaviour differences between detectors coming from the same fabrication process (see e.g. (Baril and Albert, 2008)) it would be interesting to check for this aspect on other H1RGs in similar conditions.

We have been able to study these clusters in detail, showing that they are directly linked to the energy yield, generating bigger clusters when more energy is available, but also that all cluster sizes are not equally

probable: in the case of the H1RG the clusters of 4 are favoured. This might be explained by an isotropic spread of the energy in the pixel.

For despiking purposes, we also checked the absence of persistence, even at short integration times on the Sofradir or even the H1RG after reset time increase up to 600 ns, which was the foremost concern. The opportunity we had to perform these tests on another detector than the flight one proved very interesting and valuable for our interpretations. The results we obtained validate the in-flight implementation of our despiking strategy, which is a major challenge of the Jovian environment as we saw with the examples of the past missions degradations. Indeed, the added transient signal from these high-energy electrons can have disastrous consequences on science interpretations by creating lines or bands where they do not exist or altering the whole shape of the continuum from what it should be.

From all these aspects the Sofradir detector appears a bit more resilient to transient signal effects than the H1RG, yet the differences are not strong enough to impact the mission scenario. Therefore, the selection of H1RG over Sofradir NGP as the flight detector for MAJIS has not been done on radiation-related issues but on dark current and readout-noise considerations.

Our attempts to evaluate the impact of the LVF that will cover the entire detector during the mission were impaired by the small amount of pixels ($\tilde{}$ 10% of the array) that were actually hit by electrons having crossed only the sapphire substrate because of high incidence angles on the edges of the detector, and by major uncertainties we had on its actual position during tests. More investigations would be needed to give quantitative results on its effect, yet no major effect was observed in our data so far: an increase or decrease in the spike rate because of this filter by a factor of 2 is ruled out, at least for high incidence angles ($> 45°$) of electrons. Some glow signal might also originate from the LVF or other parts of the detector housing: we saw no detectable evidence of such emission.

We have concluded this work by a test in real conditions of the despiking algorithm to be applied to MAJIS data: the foreseen despiking strategies yield down to 0.3% remaining spikes in environment conditions above the average expected around Jupiter but 3 times lower than the worst case. This work also opens the possibility of result synergies between JUICE radiation probing instruments and imagers such as MAJIS as proven by the recent study on Galileo/SSI data by (Carlton et al., 2019). Indeed, some of the unprocessed MAJIS images might be retrieved and a characterization of the spikes with similar tools as what has been presented here would bring additional data to the teams of the radiation probing instruments.

Acknowledgements

The authors would like to thank the whole MAJIS team and especially the IAS engineering team without whom those tests would not have been implemented. We acknowledge financial support from Prodex grant PEA 4000115321 with support from Belspo for Belgium, and from CNRS and CNES for France, under grants 131 425/00 and 180117.

Appendix A. Supplementary data

Supplementary data to this article can be found online at https://doi.org/10.1016/j.pss.2019.104782.

References

Bagenal, F., Dowling, T., McKinnon, W., 2006. Jupiter, the Planet, Satellites and Magnetosphere. Cambridge Planetary Science, Cambridge.

Baril, M.R., Albert, L., 2008. Characterization of persistence in WIRCam's Hawaii 2-RG arrays. In: High Energy, Optical, and Infrared Detectors for Astronomy III, vol 7021, p. 702121. https://doi.org/10.1117/12.789648 of Society of Photo-Optical Instrumentation Engineers (SPIE) Conference Series.

Becker, H.N., Alexander, J.W., Elliott, T., 2005. High-energy electron testing of CCDs for a Jovian science mission. In: Grycewicz, T.J., Marshall, C.J. (Eds.), Focal Plane Arrays for Space Telescopes II, vol 5902, pp. 171–181. https://doi.org/10.1117/12.623690 of Society of Photo-Optical Instrumentation Engineers (SPIE) Conference Series.

Beletic, J.W., Blank, R., Gulbransen, D., Lee, D., Loose, M., Piquette, E.C., Sprafke, T., Tennant, W.E., Zandian, M., Zino, J., 2008. Teledyne Imaging Sensors: infrared imaging technologies for astronomy and civil space. In: High Energy, Optical, and Infrared Detectors for Astronomy III, vol 7021, p. 70210H. https://doi.org/10.1117/12.790382 of Society of Photo-Optical Instrumentation Engineers (SPIE) Conference Series.

Carapelle, A., Grodent, D., Langevin, Y., Carter, J., Arondel, A., Vincendon, M., Guiot, P., Retherford, K., Davis, M., Liebecq, S., Renotte, E., 2019. New low electron flux facility in the 0-3.5 MeV range for the study of induced signal in JUICE instruments: UVS and MAJIS measurements. Nucl. Instrum. Methods Phys. Res. B 440, 197–200. https://doi.org/10.1016/j.nimb.2018.04.029.

Carlson, R.W., Weissman, P.R., Smythe, W.D., Mahoney, J.C., 1992. Near-infrared mapping spectrometer experiment on galileo. SSR 60, 457–502. https://doi.org/10.1007/BF00216865.

Carlton, A., de Soria-Santacruz Pich, M., Kim, W., Jun, I., Cahoy, K., 2019. Using the galileo solid-state imaging instrument as a sensor of Jovian energetic electrons. IEEE Trans. Nucl. Sci. 66, 255–261. https://doi.org/10.1109/TNS.2018.2883985.

Chorier, P., Tribolet, P.M., 2001. High-performance HgCdTe SWIR detector development at SOFRADIR. In: Andresen, B.F., Fulop, G.F., Strojnik, M. (Eds.), Infrared Technology and Applications XXVII, vol 4369, pp. 698–712. https://doi.org/10.1117/12.445350 of Society of Photo-Optical Instrumentation Engineers (SPIE) Conference Series.

Cosslett, V., Thomas, R., 1964. Multiple scattering of 5-30 kev electrons in evaporated metal films ii: range-energy relations. Br. J. Appl. Phys. 15 (11), 1283.

Cunningham, N.J., Spencer, J.R., Feldman, P.D., Strobel, D.F., France, K., Osterman, S.N., 2015. Detection of Callisto's oxygen atmosphere with the Hubble space telescope. Icarus 254, 178–189. https://doi.org/10.1016/j.icarus.2015.03.021.

de Kleer, K., Brown, M.E., 2018. Europa's optical aurora. Astron. J. 156 (4), 167. https://doi.org/10.3847/1538-3881/aadae8 arXiv:1809.04617.

ESA, J. Team, 2015. Juice Environment Specification. ESA ESTEC Noordwijk reference JS-14-09.

Fieque, B., Chorier, P., Lamoure, A., Offranc, O., 2019. Status of space activity and science detectors development at Sofradir. In: International Conference on Space Optics - ICSO 2018, vol 11180, p. 111803E. https://doi.org/10.1117/12.2536041 of Society of Photo-Optical Instrumentation Engineers (SPIE) Conference Series.

Hibbitts, C.A., McCord, T.B., Hansen, G.B., 2000. Distributions of CO_2 and SO_2 on the surface of Callisto. J. Geophys. Res. 105, 22541–22558. https://doi.org/10.1029/1999JE001101.

Kanaya, K.a., Okayama, S., 1972. Penetration and energy-loss theory of electrons in solid targets. J. Phys. D Appl. Phys. 5 (1), 43.

Klaasen, K.P., Belton, M.J., Breneman, H.H., McEwen, A.S., Davies, M., Sullivan, R.J., Chapman, C.R., Neukum, G., Heffernan, C.M., Harch, A.P., et al., 1997. Inflight performance characteristics, calibration, and utilization of the galileo solid state imaging camera. Opt. Eng. 36 (11), 3001–3028.

Kollmann, P., Roussos, E., Paranicas, C., Woodfield, E.E., Mauk, B.H., Clark, G., Smith, D.C., Vandegriff, J., 2018. Electron acceleration to MeV energies at Jupiter and Saturn. J. Geophys. Res. (Space Phys.) 123, 9110–9129. https://doi.org/10.1029/2018JA025665.

Langevin, Y., Piccioni, G., Filacchione, G., Poulet, F., Dumesnil, C., 2018. MAJIS, the VIS-IR imaging spectrometer of JUICE. In: IPM 2018, p. E1.

Lopes, R.M.C., Spencer, J.R., 2007. Io after Galileo. Springer Praxis, Chichester, UK.

L' Annunziata, M.F., 2012. Handbook of Radioactivity Analysis. Academic press.

McCord, T.B., Hansen, G.B., Clark, R.N., Martin, P.D., Hibbitts, C.A., Fanale, F.P., Granahan, J.C., Segura, M., Matson, D.L., Johnson, T.V., Carlson, R.W., Smythe, W.D., Danielson, G.E., 1998. Non-water-ice constituents in the surface material of the icy Galilean satellites from the Galileo near-infrared mapping spectrometer investigation. J. Geophys. Res. 103, 8603–8626. https://doi.org/10.1029/98JE00788.

McCullough, P., et al., 2009. Radioactivity in HgCdTe devices: potential source of "snowballs". Instrument Science Report WFC3 44, 12–56.

McGrath, M.A., Jia, X., Retherford, K., Feldman, P.D., Strobel, D.F., Saur, J., 2013. Aurora on ganymede. J. Geophys. Res. (Space Phys.) 118 (5), 2043–2054. https://doi.org/10.1002/jgra.50122.

Offenberg, J.D., Sengupta, R., Fixsen, D.J., Stockman, P., Nieto-Santisteban, M., Stallcup, S., Hanisch, R., Mather, J.C., 1999. Cosmic ray rejection with NGST. In: Mehringer, D.M., Plante, R.L., Roberts, D.A. (Eds.), Astronomical Data Analysis Software and Systems VIII, vol 172, p. 141 of Astronomical Society of the Pacific Conference Series.

Pickel, J.C., Reed, R.A., Ladbury, R., Marshall, P.W., Jordan, T.M., Gee, G., Fodness, B., McKelvey, M., McMurray, R., Ennico, K., McCreight, C., Waczynski, A., Polidan, E.J., Johnson, S.D., Weller, R.A., Mendenhall, M.H., Schrimpf, R.D., 2005. Transient radiation effects in ultra-low noise HgCdTe IR detector arrays for space-based astronomy. IEEE Trans. Nucl. Sci. 52, 2657–2663. https://doi.org/10.1109/TNS.2005.860732.

Prieskorn, Z., Griffith, C.V., Bongiorno, S.D., Falcone, A.D., Burrows, D.N., 2013. Characterization of Si hybrid CMOS detectors for use in the soft X-ray band. Nucl. Instrum. Methods Phys. Res. 717, 83–93. https://doi.org/10.1016/j.nima.2013.03.057 arXiv:1303.6666.

Raftari, B., Budko, N., Vuik, K., 2018. A modified and calibrated drift-diffusion-reaction model for time-domain analysis of charging phenomena in electron-beam irradiated insulators. AIP Adv. 8 (1), 015307.

Schenk, P.M., 2002. Thickness constraints on the icy shells of the galilean satellites from a comparison of crater shapes. Nature 417 (6887), 419.

Serra, B., Secroun, A., Clémens, J.C., Lagier, P., Niclas, M., Caillat, L., Rodriguez-Ferreira, J., Gillard, W., Tilquin, A., Ealet, A., Barbier, R., Kubik, B., Smadja, G., Ferriol, S., Prieto, E., Maciaszek, T., Norup Sorensen, A., 2015. Characterization of

Euclid-like H2RG IR detectors for the NISP instrument. In: Optics for EUV, X-Ray, and Gamma-Ray Astronomy VII, vol 9602, p. 96020G. https://doi.org/10.1117/12.2188439 of Society of Photo-Optical Instrumentation Engineers (SPIE) Conference Series.

Simms, L., et al., 2010. Hybrid CMOS SiPIN detectors as astronomical imagers. Proquest Dissertations And Theses 2010 of the Stanford University, California Section 0212 (Part 0606). AAT 3395872.

Taylor, L.S., et al., 1970. ICRU Report 16. International Commission on Radiation Units and Measurements, Washington, DC os9 (1). https://doi.org/10.1093/jicru/os9.1.Report16.

Wagner, R.J., Stephan, K., Schmedemann, N., Werner, S.C., Hoffmann, H., Roatsch, T., Kersten, E., Jaumann, R., Palumbo, P., 2018. The large bright ray crater osiris on ganymede: its age, role as a potential time-stratigraphic marker, and target for detailed imaging by the juice/janus camera. In: European Planetary Science Congress, 12.